Massachusetts Institute of Technology
Department of Electrical Engineering and Computer Science

Proposal for Thesis Research in Partial Fulfillment of the Requirements for the Degree of Master of Science

TITLE:	Joint Image Formation and Anisotropy Characterization in Wide-angle SAR
SUBMITTED BY:	Kush R. Varshney
	70 Pacific Street, Apt. 924B
	Cambridge, MA 02139-4240

_____
(SIGNATURE OF AUTHOR)

DATE OF SUBMISSION:	July 7, 2005
EXPECTED DATE OF COMPLETION:	April 1, 2006
LABORATORY:	LIDS

BRIEF STATEMENT OF THE PROBLEM:

The proposed research applies an inverse problem framework to the characterization of anisotropy in wide-angle synthetic aperture radar (SAR) imaging. Anisotropic point scatterers have scattering behavior that is a function of the angle of observation. The inverse problem, which falls out of the representation of angle-dependent scattering behavior with an overcomplete basis, is solved for multiple point scatterers jointly as an optimization with sparsifying regularization and has given promising results thus far. An approximate algorithm to solve the inverse problem using hill-climbing search with appropriate stopping conditions and search heuristics is developed, also giving promising results. Directions for further research are detailed, including improved approximate algorithms, the use of object-level information, and theoretical analysis.

SUPERVISION AGREEMENT:

The program outlined in this proposal is adequate for a Master's thesis. The supplies and facilities required are available, and I am willing to supervise the research and evaluate the thesis report.

SIGNED: _____   DATE: _____
DR. MÜJDAT ÇETIN
RESEARCH SCIENTIST, LIDS

SIGNED: _____   DATE: _____
DR. JOHN W. FISHER III
PRINCIPAL RESEARCH SCIENTIST, CSAIL

1 Introduction

Synthetic aperture radar (SAR) is an ingenious and powerful sensing modality, operable at night and through clouds, that produces high-resolution ground images for use in applications such as surveillance and remote sensing. In the proposed research, the problem of characterizing anisotropic scattering in wide-angle SAR will be investigated.

1.1 Problem motivation

Imaging with radar is accomplished by transmitting pulses of electromagnetic energy towards the scene of interest and studying the received reflections of those pulses. Return signals give information about the scene in range, i.e. distance in the direction of transmission, by using the known propagation speed and the measured round-trip time of the pulse to calculate distance. The ability to distinguish details in cross-range, the direction perpendicular to range, is proportional to the wavelength of the radar pulses divided by aperture size, the physical length of the radar antenna.

Aperture size cannot be increased beyond practically feasible dimensions and radars operate in certain frequency bands, so there is no obvious way to improve cross-range resolution. SAR overcomes the resolution limit by synthetically forming a long aperture from pulses transmitted and received over a distance. The physical layout of the SAR imaging system uses a radar mounted on an aircraft in flight. As the aircraft proceeds along its flight path, it transmits radar pulses towards the ground and receives the reflected pulses. The length of the flight path becomes the length of the synthetic aperture; lengthening the flight path improves the cross-range resolution. In spotlight-mode SAR, the radar is steered so that it always looks towards a single patch on the ground from every point along its flight path. Pulses are transmitted to and received from the ground patch at equally spaced aspect angles. Accurate knowledge of aircraft location is essential for SAR image formation.

Advances in navigation technologies and avionics now allow the synthesis of longer apertures than ever before, and consequently more finely resolved images. A problem that arises with long, or wide-angle, apertures is that dependence of scattering behavior on aspect angle, termed *anisotropy*, becomes prominent because objects are viewed from different sides rather than from nearly the same point of view in the narrow-angle case. For example, a mirror or flat metal sheet may reflect strongly when viewed straight on, but barely reflect at all from an oblique angle. Anisotropy characterization may be used as a feature for automatic target recognition, such as to discriminate an isotropic tree trunk, reflecting the same from all directions, and the anisotropic flat metal side of a truck. It may also be used for improved image formation.

1.2 Contributions

This proposal puts forth an inverse problem formulation utilizing an overcomplete basis and sparsifying regularization for joint image formation and anisotropy characterization in wide-angle SAR. A similar approach has been used for source localization in array processing [15], but has not previously been applied to characterizing anisotropy in SAR. One general principle in previous work on the anisotropy problem has been to divide the full wide-angle aperture into smaller subapertures and form a sequence of subaperture images with inherently reduced cross-range resolution for use in further processing. Another general principle has been to develop parametric models for angle-dependent scattering behavior. The proposed methodology does not suffer a reduction in resolution because the entire available aperture is used and is more flexible than parametric models. Additionally, the proposed framework solves for multiple spatial locations jointly, ameliorating the ill-effects of close proximity neighboring scatterers [13]. The preliminary work that has led to this proposal has indicated that the inverse problem framework has potential, but is also memory and computation intensive. In this light, a graph-structured interpretation leading towards approximate algorithms to solve the inverse problem is also proposed. The graph structure paradigm may well find application in a wide variety of sparse signal representation settings beyond the specific problem of anisotropy in SAR. Image formation techniques have been developed for various specific modalities, but work on fully general methods applicable to any given sensor modality is far from developed [18]. It is hoped that the proposed

research will lead to algorithms and techniques useful for synthetic aperture radar imaging as well as other imaging scenarios.

1.3   Organization of the proposal

The proposal is organized as follows. The second section details the observation model for spotlight-mode SAR, which will be used throughout the proposed work. The third section reviews inverse problems and the use of regularization to find meaningful solutions, while the fourth section summarizes previous work done on the characterization of anisotropic scattering. The fifth section discusses the proposed approach. The inverse problem and regularization framework is set up for use in characterizing anisotropy and some preliminary results on synthetic data are presented. The sixth section discusses approximations to the method given in the fifth section; in particular, a graph-structured approach is motivated and preliminary results are given, also on synthetic data. In the last section, future directions of the research are articulated along with a timeline, and list of principal equipment, facility, and data needs.

2   Synthetic Aperture Radar Observation Model

Spotlight-mode SAR, a tomographic observation process [17], is modeled similarly to other imaging modalities such as magnetic resonance imaging, acoustic microscopy, and positron emission tomography. The rudiments of the SAR model are presented below; a more thorough description may be found in [11], among many others.

2.1   Scattering function and phase history

The scattering from each point of the ground patch under observation is manifested as an amplitude scaling and phase shift that can be expressed as a complex number. Thus, scattering from the entire ground patch can be characterized by a complex-valued function of two spatial variables $s(x, y)$, which will be referred to in some instances as the *scattering function* and in others as the *image*. Due to the design of the radar pulse and the physics of the observation process, the collection of received signals is not $s(x, y)$ directly. If the received signal at a particular angle θ is denoted $r_\theta(t)$, the scattering function is defined on a circular ground patch with radius L (with x and y coordinates on the ground), and c is the speed of propagation, then:

$$r_\theta(t) = \iint_{x^2+y^2 \leq L^2} s(x, y) \exp\left\{-j\frac{4\pi f(t)}{c}(x\cos\theta + y\sin\theta)\right\} dxdy. \tag{1}$$

The time dependence in the received signal and the frequency variable $f(t)$ is often suppressed, yielding:

$$r_\theta = \iint_{x^2+y^2 \leq L^2} s(x, y) \exp\left\{-j\frac{4\pi f}{c}(x\cos\theta + y\sin\theta)\right\} dxdy, \tag{2}$$

which incidentally can be recognized as a Fourier transform. Collectively, the received signals from all angles are the Fourier transform of $s(x, y)$, over finite support and sampled at equally spaced angles. To allow digital processing, the received signals are also sampled in frequency. This collected data is known as the *phase history*.

2.2   Point scatterers

The scattering response of objects such as vehicles on the ground can be approximated as the sum of responses from point scatterers when using high frequencies [12]. When considering the scattering function of a single point located at (x_m, y_m), the radius of the ground patch L goes to zero and the received signal goes to:

$$s(x_m, y_m) \exp\left\{-j\frac{4\pi f}{c}(x_m\cos\theta + y_m\sin\theta)\right\}. \tag{3}$$

Since the total scattering is the sum of all point scatterers, the received signal, with N_s point scatterers, is:

$$r_\theta = \sum_{m=1}^{N_s} s\left(x_m, y_m\right) \exp\left\{-j\frac{4\pi f}{c}\left(x_m \cos\theta + y_m \sin\theta\right)\right\}. \tag{4}$$

2.3 Anisotropy

In the preceding exposition, an implicit assumption was made that the scattering function $s\left(x, y\right)$ is not dependent on aspect angle, which as discussed in Sec. 1, is not valid in the wide-angle case. In fact, scattering behaviors are dependent both on the aspect angle and the frequencies in the radar pulse. The scattering function should be written explicitly as $s\left(x, y, f, \theta\right)$ to capture the dependencies. In conventional imaging, the failure to model frequency dependence and angle dependence results in an averaging over those variables, leading to inaccurate reflectivity estimates. In wide-angle imaging, angle-dependence is more prominent than frequency-dependence, so it will be the focus of the proposed research. Tools developed for the characterization of anisotropy ought to be useful for characterizing frequency dependence as well. In this work, it will be assumed that the scattering function is not dependent on frequency. In total, with N_f frequency samples and N_θ angle samples, the model for the phase history that will be used is:

$$r\left(f, \theta\right) = \sum_{m=1}^{N_s} s\left(x_m, y_m, \theta\right) \exp\left\{-j\frac{4\pi f}{c}\left(x_m \cos\theta + y_m \sin\theta\right)\right\},$$

$$f = f_1, \ldots, f_{N_f}, \theta = \theta_1, \ldots, \theta_{N_\theta}. \tag{5}$$

3 Inverse Problems

In inverse problems, one has observations, possibly noisy, and attempts to discover the cause of those observations. In mathematical notation, $\mathbf{g} = \mathbf{T}\left(\mathbf{f}\right) + \mathbf{n}$ is to be solved, where $\mathbf{f}$ is the unknown, $\mathbf{g}$ is the observed data, $\mathbf{T}$ is the observation process, and $\mathbf{n}$ is noise.

3.1 Ill-posed inverse problems and regularization

Issues with solving inverse problems are that a solution may not exist, that there may be no unique solution such as when the null space of $\mathbf{T}$ is not empty, or that the solution may not be stable when the observation is perturbed. Such conditions make the problem ill-posed. Regularization — the inclusion of prior knowledge to stabilize the solution in the presence of noise and to give meaningful and reasonable estimates — is used to deal with these issues when estimating $\mathbf{f}$ from $\mathbf{g}$.

Now, restricting $\mathbf{T}$ to be a linear operator, $\mathbf{f} \in \mathbb{C}^M$, and $\mathbf{n}, \mathbf{g} \in \mathbb{C}^N$, the problem becomes:

$$\mathbf{g} = \mathbf{T}\mathbf{f} + \mathbf{n}, \mathbf{T} \in \mathbb{C}^{N\times M}. \tag{6}$$

The standard minimum norm least-squares solution for $\mathbf{f}$ may not be meaningful or may be inappropriate for the application at hand. One approach to solving the inverse problem with regularization is to construct a cost function of the form:

$$J\left(\mathbf{f}\right) = J_1\left(\mathbf{f}\right) + \alpha J_2\left(\mathbf{f}\right), \tag{7}$$

where J_1 is a data fidelity term, often $\|\mathbf{g} - \mathbf{T}\mathbf{f}\|_2^2$; J_2 is a regularization term; and α is a regularization parameter that trades off data fidelity and regularization. The $\mathbf{f}$ that minimizes the cost function is the desired solution to the inverse problem. When $\alpha = 0$, the cost function reduces back to least-squares.

3.2 Regularization methods

In one approach to regularization developed by Tikhonov, the regularization term is quadratic, i.e. $J_2(\mathbf{f}) = \|\mathbf{f}\|_2^2$. This method and other quadratic regularization methods are tractable and have closed form solutions, but may not necessarily fit the application. The solutions resulting from quadratic regularization are 'smooth,' i.e. the elements of $\mathbf{f}$ vary smoothly.

Certain non-quadratic regularization methods allow less smooth solutions. If the regularization term is chosen appropriately, a sparse solution can be obtained that has few (or just one) non-zero entries. One such example is the non-convex ℓ_p-quasi-norm: $J_2 = \|\mathbf{f}\|_p^p = \sum_i |f_i|^p$, with $p < 1$. When $p = 0$, the cost simply counts the number of non-zero elements of $\mathbf{f}$. There is no closed form solution for this cost function, but the optimization can be performed with a half-quadratic method detailed in [4]. This form of regularization will be used in the proposed research.

In some settings, $\mathbf{T}$ is a basis set for representing $\mathbf{g}$, and $\mathbf{f}$ is a vector of coefficients into the basis. For example, consider $\mathbf{T}$ to be the standard basis $[\mathbf{e}_1 \ \mathbf{e}_2 \ \cdots \ \mathbf{e}_M]$ and $\mathbf{g}$ to be any arbitrary vector in $\mathbb{R}^M$. Then $\mathbf{f}$ is the vector of coordinates for $\mathbf{g}$ in this Euclidean space. While this example is trivial because $\mathbf{T} = \mathbf{I}$, and $\mathbf{f} = \mathbf{g}$, it illustrates that an orthogonal, minimum-spanning basis has a unique $\mathbf{f}$ for each $\mathbf{g}$ and that solving for $\mathbf{f}$ is not ill-posed. All elements of $\mathbf{f}$ must potentially be non-zero to represent $\mathbf{g}$. However, if $\mathbf{T}$ is an overcomplete basis set (there are more basis vectors than the dimension of $\mathbf{g}$), then there is no unique $\mathbf{f}$ for each $\mathbf{g}$ and the problem becomes ill-posed. Of the multitude of possible solutions, sparse ones easily lend themselves to natural interpretation in many contexts. Thus in solving inverse problems with overcomplete bases, sparse solutions are often meaningful and should be favored through regularization in those contexts.

4 Methods for Characterizing Anisotropic Scattering

The problem of detecting, estimating, and modeling aspect-dependent scattering behavior has received attention lately. A few proposed methods will be discussed in this section. Some methods operate in the image domain, while others operate in the phase history domain.

4.1 Image domain methods

Image domain methods use a multiaperture approach for characterizing anisotropy. The phase history is divided into smaller pieces, with cuts along the θ axis. An image, known as a subaperture image, is then formed from each piece of the phase history. It should be noted that the subaperture images have poorer cross-range resolution than an image formed from the full aperture would. Also, subapertures are of fixed angular extent; consequently, any subaperture analysis is limited in its ability to characterize anisotropy extent.

In [9], the division of the aperture is a partition into equally-sized subapertures and the goal is the detection of anisotropy. After subaperture images are formed through conventional imaging and registered, changes among corresponding pixels are detected. In essence, the procedure is like looking at a flipbook and picking out little flashes. The detection is posed as a binary hypothesis testing problem for each location and the likelihood functions are estimated using a trained hidden Markov model. The result can be summarized as a Boolean image that is true at pixel (x_n, y_n) if $s(x_n, y_n, \theta)$ is anisotropic. By dividing the aperture into non-overlapping subapertures, anisotropic behavior that straddles a subaperture boundary may be missed. Overlapped subapertures are not used in [9] due to the increase in computation. Similar methods are described in [20].

The method described above can be visualized as passing the phase history through a filterbank with non-overlapping rectangular windows. A different procedure for forming subapertures, given in [16], is to use a filterbank with overlapping Hamming windows. Further processing used in [16] involves subaperture image formation using point-enhanced imaging [4]. Anisotropy is characterized by considering corresponding pixels in each subaperture image — the subaperture image with the maximum pixel value corresponds to the direction of anisotropy. Other approaches use filters different from Hamming and rectangular windows

in the filterbank that are matched to expected responses [1]. Other subaperture approaches are detailed in [14],[8].

Both of the above methods consider anisotropy of fixed angular extent only. A method of detecting anisotropic scattering [13] that is in the same spirit as the previous methods additionally uses multiple levels of subapertures. Within each level, the subapertures have the same angular extent and are overlapping, but the extent in each level is half that of the previous level. The layers of subapertures form a tree-structured subaperture pyramid, with the full aperture as the root. Each of the subapertures can be considered as a hypothesis. For each pixel (x_n, y_n) independently, the tree is searched for the best hypothesis to explain the data, considering two levels at a time, starting at the root. The search is continued if a child subaperture is more likely to explain the data than the parent. The likelihoods are obtained using a derived statistic analogous to the total energy contained in the subaperture.

The above framework, with many hypotheses, moves towards allowing a continuum of aspect angle extents, but is still limited to full-, half-, quarter-, $\cdots$-, apertures. All of the image domain methods use subapertures which inherently reduce resolution. Also, in most of the techniques, the characterization of anisotropy in different spatial locations (different pixels) is done independently.

4.2   Phase history domain methods

A different approach to the characterization of anisotropic scattering is to choose a parametric model for $s(x_m, y_m, \theta)$ and estimate the model parameters. A number of these parametric models are given below. A model obtained from the geometrical theory of diffraction is:

$$s(x_m, y_m, f, \theta) = A_m \left(\frac{jf}{f_c}\right)^{\alpha_m} \exp\{\beta_m \theta\} \tag{8}$$

where f_c is the center frequency of the radar pulse, and A_m, α_m, and β_m are the parameters to estimate [19]. Two other parametric models also motivated by the geometrical theory of diffraction [10] include, for localized scattering mechanisms such as corners and edges of manmade objects:

$$s(x_m, y_m, f, \theta) = A_m \exp\{-2\pi f \gamma_m \sin\theta\} \tag{9}$$

and for distributed scattering mechanisms, such as flat plates and cylinders:

$$s(x_m, y_m, f, \theta) = A_m \left(\frac{jf}{f_c}\right)^{\alpha_m} \operatorname{sinc}\left(\frac{2\pi f}{c} L_m \sin(\theta - \varphi_m)\right). \tag{10}$$

The parameters to be estimated are A_m, α_m, γ_m, L_m, and φ_m. Iterative algorithms for maximum likelihood parameter estimation for these three models exist [5].

A different parametric model for scattering behavior uses an expansion of $s(x, y, \theta)$ into spherical harmonic functions with θ as their argument [6]. The coefficients for the spherical harmonic basis are obtained by taking inner products. In [21], the scattering function is parameterized with Gaussians. The model is:

$$s(x_m, y_m, \theta) = A_m \exp\left\{-\frac{(\theta - \varphi_m)^2}{2\sigma_m^2}\right\} \tag{11}$$

and the parameters A_m, φ_m, and σ_m are found with a given efficient numerical algorithm.

The parametric model formulation of the anisotropy characterization problem is of course predicated on the correct modeling of natural phenomena. The above parametric models often do not hold in the wide-angle scenario [16]. Model misspecification error is considered in [5], but with the limitation that the unknown true model is of a known parametric family. However, moving from narrow-angle SAR to wide-angle SAR is not simply a transition of the parametric model within a family of models.

5 Sparsifying regularization framework for anisotropy characterization

A framework different from the subaperture and parametric formulations discussed in the previous section is now proposed. The anisotropy characterization problem is approached through the inverse problem and regularization framework described in Sec. 3 by constructing an overcomplete basis and appropriately using the phase history data. The idea is to expand the scattering function $s(\theta)$ at each spatial location as a superposition of basis vectors. The set of available basis vectors for this expansion contains many more vectors than the dimension of θ, chosen in such a way that linear combinations of very few of them accurately represent plausible angle-dependent scattering behaviors. The problem of determining the scattering behavior at all spatial locations is then a matter of determining the small number of basis vectors and their scale factors at each location. After laying the foundation for the approach, including the specific choice for the overcomplete basis used thus far, some results will be presented to demonstrate its efficacy.

5.1 Overcomplete basis and observations

As seen in Sec. 4, methods employing subaperture analysis and parametric models expect to find contiguous intervals in θ for which there is non-zero scattering. Basis vectors in the proposed framework are chosen to similarly represent contiguous segments of anisotropy. The overcomplete basis is constructed as follows, first considering a single frequency f_k and a single spatial location (x_m, y_n). In order to discover angle-dependent scattering, basis vector i has the form:

$$b_i(\theta) \exp\left\{-j\frac{4\pi f_k}{c}(x_m \cos\theta + y_n \sin\theta)\right\},$$

with N_θ elements. The functions $b_i(\theta)$ are chosen to be rectangular pulses with all possible angular extents and all possible starting angles; other pulse shapes may be considered in future work. For example, if $N_\theta = 8$, then $\mathbf{b}_1 = [1\ 1\ 1\ 1\ 1\ 1\ 1\ 1]^T$, $\mathbf{b}_2 = [1\ 1\ 1\ 1\ 1\ 1\ 1\ 0]^T$, $\mathbf{b}_3 = [0\ 1\ 1\ 1\ 1\ 1\ 1\ 1]^T$, and the final rectangular pulse $\mathbf{b}_M = [0\ 0\ 0\ 0\ 0\ 0\ 0\ 1]^T$. The basis vectors are of unit amplitude; solving the inverse problem gives the complex amplitude coefficients. The full basis set for $N_\theta = 8$ is illustrated in Fig. 1. The dots represent entries that have a value $\in \mathbb{C}$, and spaces without dots represent zero-valued elements. The matrix composed
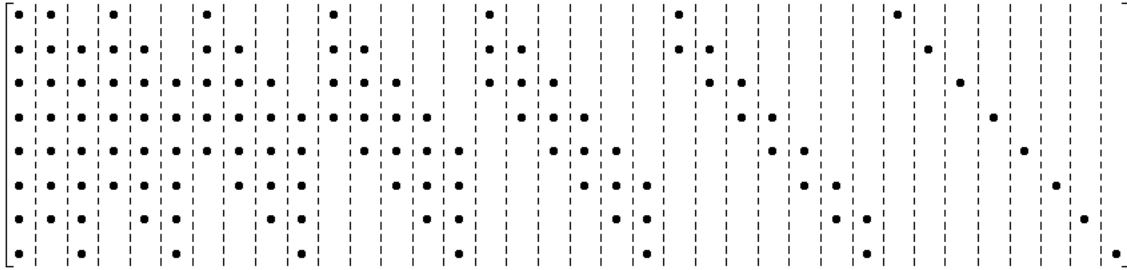

Figure 1: Illustration of matrix $\mathbf{T}_{k,p}$ for $N_\theta = 8$.

of the basis set is denoted $\mathbf{T}_{k,p}$, where $p = (m, n)$. There is a simple relationship between the number of basis vectors M and the number of angle samples. M is the N_θ^{th} triangular number:

$$M = \binom{N_\theta + 1}{2} = \frac{1}{2}N_\theta^2 + \frac{1}{2}N_\theta. \tag{12}$$

The basis is overcomplete because $M > N_\theta$ (for $N_\theta > 1$).

Moving to the general case of K frequencies and P spatial locations, the basis becomes:

$$\mathbf{T} = \begin{bmatrix} \mathbf{T}_{1,1} & \mathbf{T}_{1,2} & \cdots & \mathbf{T}_{1,P} \\ \mathbf{T}_{2,1} & \mathbf{T}_{2,2} & \cdots & \mathbf{T}_{2,P} \\ \vdots & \vdots & \ddots & \vdots \\ \mathbf{T}_{K,1} & \mathbf{T}_{K,2} & \cdots & \mathbf{T}_{K,P} \end{bmatrix}. \tag{13}$$

By forming this big $\mathbf{T}$ matrix, with dimension $(N_\theta \cdot K) \times (M \cdot P)$, the spatial locations are treated jointly. The observation vector $\mathbf{g}$ of Sec. 3 must be similarly constructed from the phase history data. If the phase history $r(f, \theta)|_{f=f_k}$ is taken as a column vector, then:

$$\mathbf{g} = \begin{bmatrix} r(f_1, \theta) \\ r(f_2, \theta) \\ \vdots \\ r(f_K, \theta) \end{bmatrix}. \tag{14}$$

5.2   Coefficient vector

With $\mathbf{T}$ and $\mathbf{g}$ thus defined, in the inverse problem setup, $\mathbf{f}$ is a length $M \cdot P$ vector of coefficients into the basis defined by $\mathbf{T}$ to be solved through regularization. For example, if the point scatterer located at the first position, $p = 1$, is isotropic with complex amplitude A, then the first entry of $\mathbf{f}$ should be A and the next $M - 1$ entries should be zero. Similarly, the second M entries of $\mathbf{f}$ depend on the second spatial location, and so on. Thus, by setting up the problem in this manner, it is possible to decompose the phase history data into contributions from different point scatterers and in the process, characterize amplitude and anisotropy for each one. As a notational convenience, $\mathbf{f}_p$ will be a length M vector of coefficients corresponding to position p. There is no requirement that all spatial locations under consideration contain a scatterer. If there is no scatterer at a particular spatial location p, then all of the elements of $\mathbf{f}_p$ should come out to be zero. It is thus possible to use a grid of pixels as the set of spatial locations.

It is apparent from the form of $\mathbf{T}$ and $\mathbf{f}$ that zero or one coefficients in each $\mathbf{f}_p$ (or very few in the case of noncontiguous anisotropy) should be non-zero. Thus, sparsifying regularization, specifically using the non-convex quasi-norm regularization term discussed in Sec. 3.2, is used to estimate $\mathbf{f}$ using a half-quadratic optimization method [4]. Some results obtained using this regularization method on simulated data with small problem size are presented in the following section.

5.3   Example

The example in this section constructs phase history measurements $\mathbf{g}$ using the SAR forward observation model $\mathbf{T}$. The solution of the inverse problem is obtained using both least-squares and sparsifying regularization. A wide-angle scenario is considered.

The example has $N_\theta = 16$ equally-spaced angle samples over $[-55°, +55°]$, resulting in $M = 136$. There are $K = 3$ frequency samples over a narrow band with frequencies 7.047 GHz, 7.059 GHz, and 7.070 GHz; the speed of propagation $c = 2.998 \times 10^8$ m/s. The number of positions $P = 25$, with spatial locations $((0,0), (0,1), \ldots, (0,4), (1,0), \ldots, (4,4))$. All in all, $\mathbf{T}$ is 48×3400, $\mathbf{f}$ is 3400×1, and $\mathbf{g}$ is 48×1.

Of the 25 positions, five contain point scatterers, with a variety of extents of anisotropy and complex amplitudes. Fig. 2 shows the underlying true coefficient vector $\mathbf{f}$ that is operated upon by $\mathbf{T}$ to generate the observations $\mathbf{g}$. There is no noise in this example. In the figure, $\mathbf{f}$ has been partitioned into subvectors $\mathbf{f}_p, p \in \{1, 2, \ldots, 25\}$, with each $\mathbf{f}_p$ arranged according to its corresponding spatial location as in an image. The 136 coefficients are displayed as a stem plot, in an ordering similar to Fig. 1, with the $\circ$ being the real part and the $\times$ being the imaginary part. The magnitude of the true scattering function is displayed in Fig. 3. In similar fashion as Fig. 2, the angle-dependent scattering behavior for each spatial location is arranged as in an image. The scattering response magnitudes of the 16 angle samples are plotted for each location. (The angle-dependent scattering for the three frequencies is equal in magnitude by construction.)
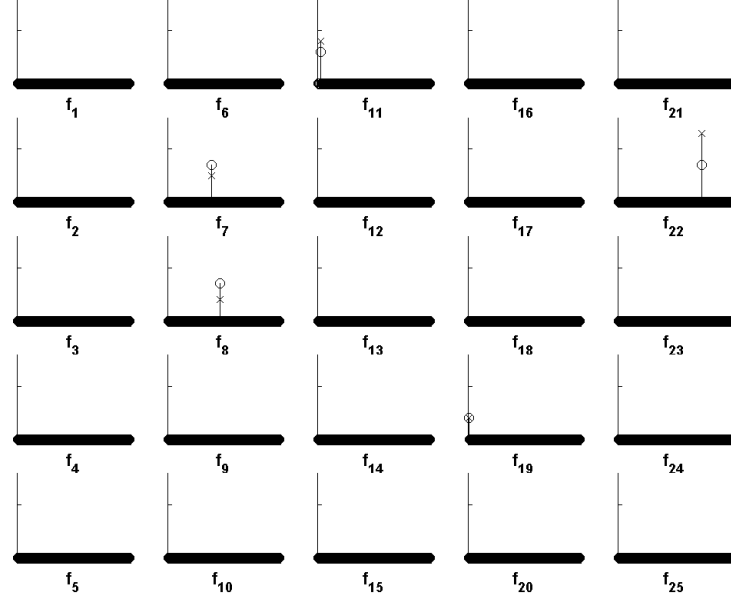
Figure 2: True coefficient vector $\mathbf{f}$ partitioned into subvectors $\mathbf{f}_p, p \in \{1, 2, \ldots, P\}, P = 25$, with real part $\circ$ and imaginary part $\times$.
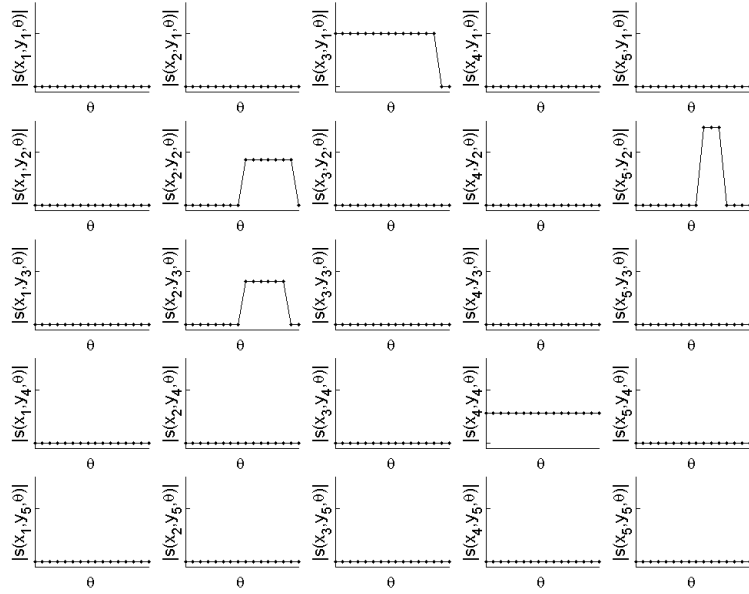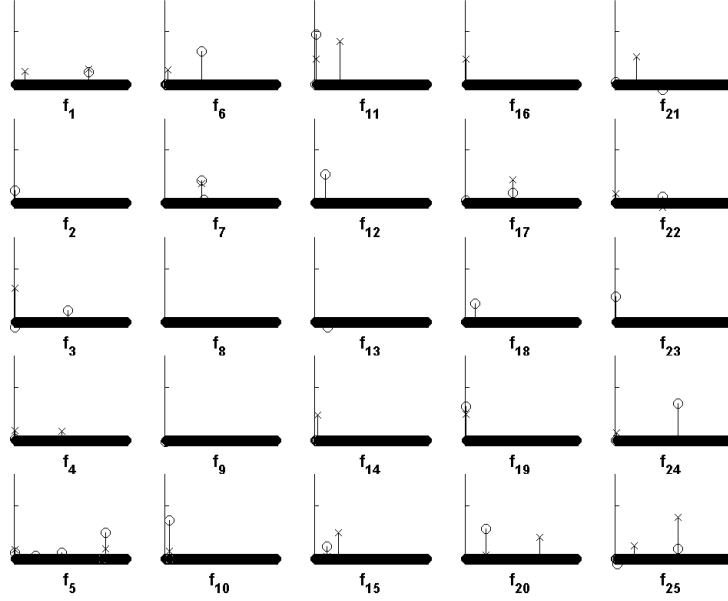

Figure 3: True scattering function magnitude.

Figure 4: Least-squares solution coefficient vector $\hat{\mathbf{f}}^{LS}$ partitioned into subvectors $\hat{\mathbf{f}}_p^{LS}, p \in \{1, 2, \ldots, P\}, P = 25$, with real part $\circ$ and imaginary part $\times$.

The inverse problem is solved first by least-squares yielding $\hat{\mathbf{f}}^{LS}$, which can be partitioned into $\hat{\mathbf{f}}_p^{LS}$. In Fig. 4, $\hat{\mathbf{f}}^{LS}$ is displayed in the same manner as $\mathbf{f}$ was displayed in Fig. 2. This solution puts energy into coefficients of all $\hat{\mathbf{f}}_p^{LS}$, giving non-zero scattering to all spatial positions as seen in Fig. 5. Of course, as there is no noise, the product of $\hat{\mathbf{f}}^{LS}$ and $\mathbf{T}$ equals $\mathbf{g}$, but in this solution, the contributions are not assigned to individual spatial locations in a way that accurately reflects the underlying truth.

In contrast, the use of sparsifying regularization gives a solution to the inverse problem that explains the observations consistent with the true scattering function. To obtain the coefficients $\hat{\mathbf{f}}^{SR}$ shown in Fig. 6, the regularization term was the $\ell_{0.1}$-quasi-norm and the regularization parameter α was 3. The scattering function corresponding to these coefficients, shown in Fig. 7, illustrates that this methodology of an overcomplete basis with sparsifying regularization is an effective method for characterizing anisotropy of point scatterers from phase history measurements.

In theory, there is no restriction on the size of the problem that this method can be applied to. However, the number of columns of $\mathbf{T}$, which is $O\left(N_\theta^2 P\right)$, is restrictive in terms of memory as well as computation in realistic imaging scenarios with hundreds of angle samples and thousands of spatial locations. In the following section, approximations to the method described and demonstrated in this section will be developed that require less memory and computation.

6 Approximate methods

The overcomplete basis considered thus far has a graph-structured interpretation that will enable approximate algorithms to be developed which reduce the combinatorial explosion in the number of columns in $\mathbf{T}$ with N_θ. A few ways to reduce the number of spatial locations also exist. Algorithms that use one approximation or use a few approximate methods together can be used to solve the inverse problem. Depending
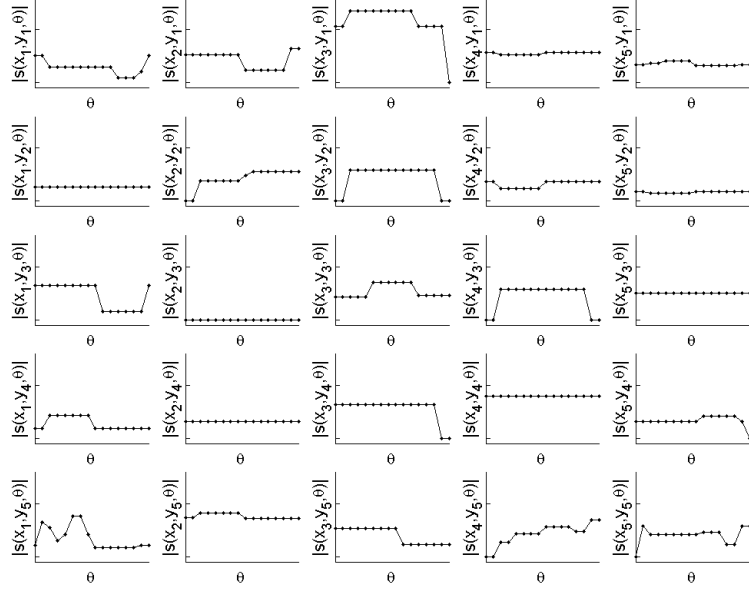
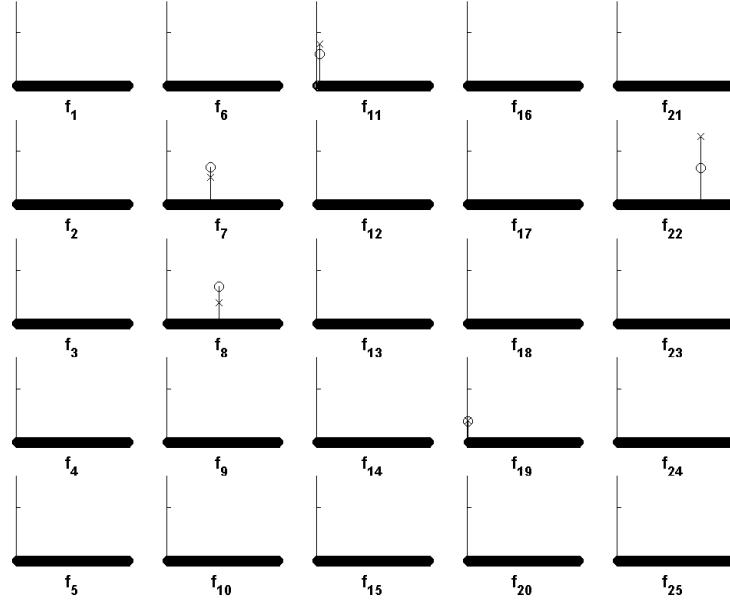Figure 5: Scattering function magnitude from least-squares solution.

Figure 6: Sparsifying regularization solution coefficient vector $\hat{\mathbf{f}}^{SR}$ partitioned into subvectors $\hat{\mathbf{f}}_p^{SR}, p \in \{1, 2, \ldots, P\}, P = 25$, with real part $\circ$ and imaginary part $\times$.
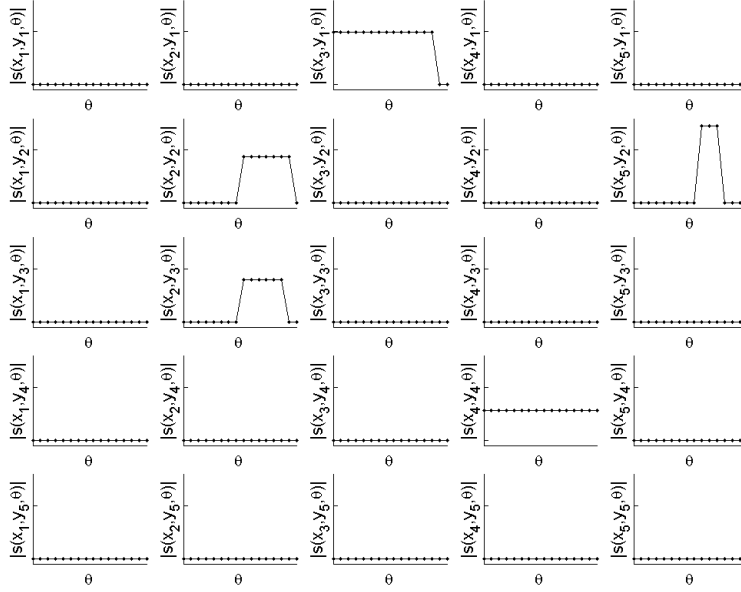
Figure 7: Scattering function magnitude from sparsifying regularization solution.

on the size of the problem and the requirements of the application, one algorithm can be selected from this suite of possible algorithms.

6.1 Graph-structured interpretation of basis

For each spatial location, the set of basis vectors in the overcomplete basis can be arranged as nodes in a weakly connected directed acyclic graph. The graph is given in Fig. 8 for $N_\theta = 8$, with nodes labeled to the left. The lowercase letter labels inside the nodes can be ignored for now. A topological sort for this graph is exactly the ordering from left to right of the vectors in $\mathbf{T}_{k,p}$, illustrated in Fig. 1. The root node is the isotropic basis vector and traversing down the graph corresponds to decreasing angular extent of anisotropy. A graph of this form with N_θ rows will be referred to as an N_θ-level *plinko graph*, after a pricing game on the daytime game show *The Price is Right*.

The inverse problem with overcomplete basis and sparsifying regularization may be reconstituted as a search on the plinko graph for one or few nodes that explain the data. If it is assumed that the anisotropy is contiguous, then the search is for one node. In addition to finding the goal node, a complex amplitude must also be determined for it.

Any directed acyclic graph can be converted to a tree through node repetition. The transformation for a 3-level plinko graph is shown in Fig. 9. Search on a tree is a well-studied problem with well-studied algorithms, with the only requirement that it should be obvious when the goal node is reached. Depth-first search and breadth-first search are two blind search algorithms that incorporate no prior information to guide the search. In heuristic search algorithms, however, some notion of closeness to the goal is available during the search process, allowing the search to proceed along paths that are likely to lead to the goal. Heuristic search algorithms have reduced average-case running time than blind search algorithms.

One example of a heuristic search algorithm is hill-climbing search, also known as guided depth-first search. In the depth-first algorithm, one path is followed from root to leaf in a predetermined way, such as:
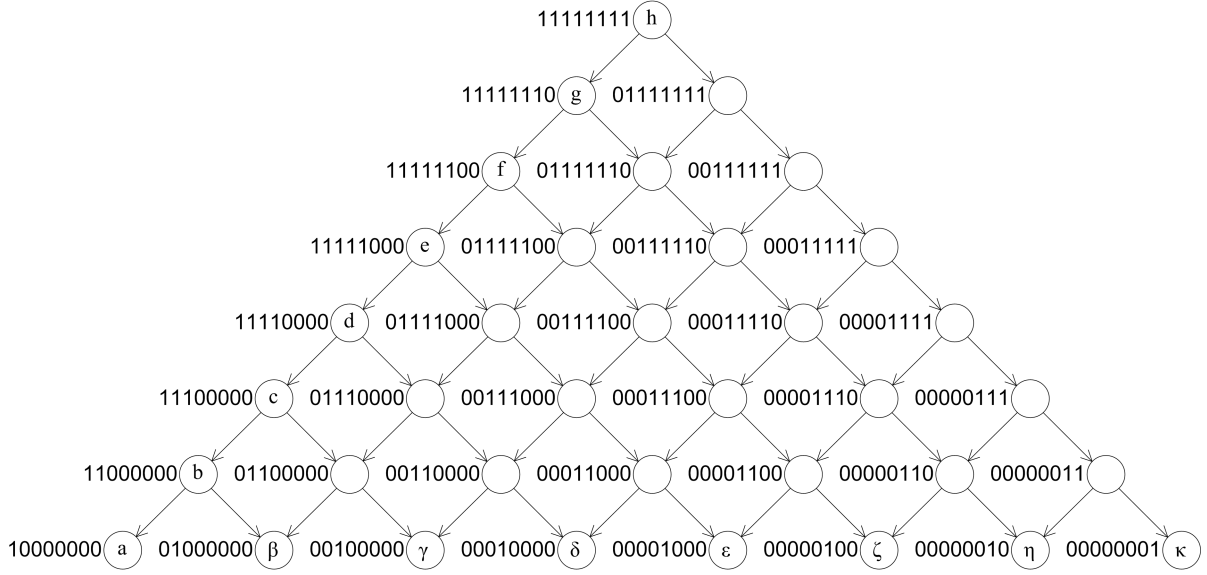
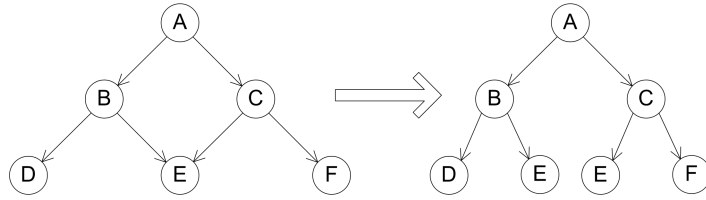Figure 8: Directed acyclic graph representation for overcomplete basis.

Figure 9: Conversion of directed acyclic graph to tree

"always proceed to the left-most child." If the goal is not found along the way and the bottom of the tree is reached, then there is back-tracking also in a predetermined way. In hill-climbing, the search still proceeds from root to leaf along one path, but this path is not predetermined. Instead of always proceeding to the left-most child, the algorithm will "proceed to the most promising child based on a heuristic." Selection of back-tracking paths also involves use of the heuristic. Both depth-first search and hill-climbing search always find the goal if it exists in the tree, but not necessarily following the shortest path from the root. In the next section, heuristics and stopping conditions will be discussed.

6.2   Search heuristics and stopping conditions

In standard search problems on trees, nodes are labeled and the goal of the search is specified with a label, e.g. "Find node K." Thus the stopping criterion for the search is simply whether the current node's label matches the goal of the search. Also, there is often a notion of intrinsic distance between nodes that leads to simple search heuristics. In a graph in which cities are represented by nodes and roads connecting those cities are represented by edges, an obvious heuristic is the distance between the cities. Consider the following example. The root node is Albany, New York, the goal of the search is Cambridge, Massachusetts, and there is no edge between the two. Albany has four child nodes: Montréal, Québec; Syracuse, New York; Newark, New Jersey; and Springfield, Massachusetts. During the search, the heuristic is distance from nodes to Cambridge. Since Springfield is closest to Cambridge using this heuristic, the path through Springfield will be chosen first to explore. Heuristic search on this type of graph often yields the shortest path, but not always, such as when roads must go around bodies of water.

When the inverse problem at hand is reformulated as a search on an N_θ-level plinko graph, stopping criteria and heuristics are not obvious. One clear desideratum is that calculation of both should be much less memory and computation intensive than solving the full problem through the framework developed in Sec. 5. An m-level plinko graph, $m \ll N_\theta$, with its root at the current node of the search, which will be called the *guiding graph*, leads to a useful heuristic and stopping condition as discussed in the rest of this section.

Intuition about the problem suggests that if the basis vector corresponding to true scattering behavior is not included in the collection of basis vectors when the inverse problem is solved in a sparsity enforcing manner, then the resulting $\hat{\mathbf{f}}$ will have a non-zero coefficient for the basis vector most "similar" to the truth. Assuming this intuition holds, if a basis only contains vectors with large angular extent and the truth is of small angular extent, then the resulting coefficients will be zero for all but the smallest of the available (though still of large angular extent) basis vectors. In terms of the N_θ-level plinko graph, if the true coefficient is far down in the graph, but the inverse problem is solved with only an m-level guiding graph having the same root as the N_θ-level plinko graph, then coefficients in the first $m-1$ levels will be zero and coefficients in level m may be non-zero. In the same vein, if the m-level guiding graph is rooted below the true coefficient, then the root coefficient may be non-zero and the coefficients in levels two through m will be zero. If the m-level guiding graph is such that it contains the true coefficient, then the true coefficient will be non-zero and the rest of the coefficients will be zero.

This intuition is confirmed through experimentation for $N_\theta = 400$, $m = 8$, and implicitly $P = 1$. The 400 angle samples are over the interval $[-55°, +55°]$, the number of frequencies $K = 3$ with the same frequency values as in Sec. 5.3, and the regularization parameter $\alpha = 150$. The 8-level guiding graph contains 36 nodes, as shown in Fig. 8. In the first experiment, with results in Fig. 10, the guiding graph is fixed with root at the left-most node of level 200 in the plinko graph. The true scattering behavior is varied from isotropic, to anisotropic with medium angular extent, to anisotropic with just one angle sample non-zero. In terms of the 400-level plinko graph, the true coefficient is varied, starting at the root node, through all nodes along the left edge of the graph, to the left-most node of level 400, as diagrammed in the left portion of Fig. 10. The large triangle is the 400-level plinko graph, the tiny filled triangle is the fixed guiding graph, and the arrows along the left edge indicate the variation of the true node. In the two plots, the angular extent of the true scattering behavior is plotted on the horizontal axis. In the top plot, the coefficient magnitudes for all 36 coefficients are plotted on the vertical axis, whereas in the bottom plot, coefficient magnitudes are indicated by shading (white is zero) and each horizontal strip is for each of the 36 different coefficients. The coefficient
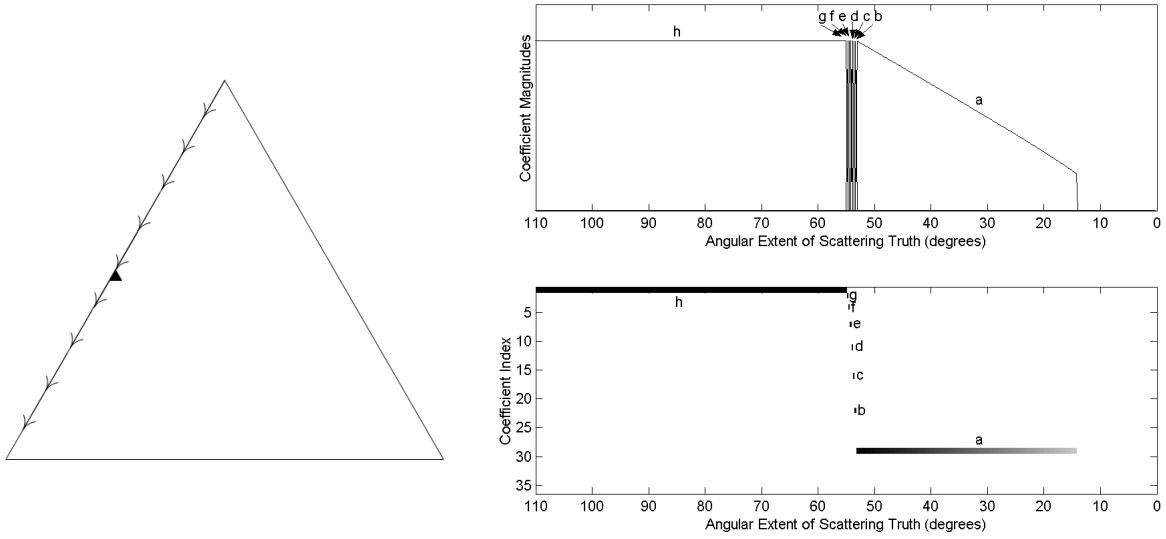
Figure 10: Coefficient magnitudes in m-level guiding graph as true scattering behavior is varied from isotropic to highly anisotropic. The m-level guiding graph is fixed with top node having angular extent $55.3°$ and m^{th} row nodes having angular extent $53.1°$.

values are obtained by solving the inverse problem with sparsifying regularization. Most coefficients are zero for all true scattering behaviors in this experiment. Lines on the plots are labeled in correspondence with node labels in Fig. 8. The figure shows that in agreement with intuition, in the regime where the guiding graph is below the true coefficient, the root node (node h) is non-zero. In the regime where the guiding graph covers the true coefficient, the correct node is non-zero. Also in agreement with intuition, when the guiding graph is above the true coefficient, the node in the last level closest to the truth (node a) is non-zero and others are zero. It should be noted that the influence of the finest angular extent scattering, when the true coefficient has angular extent less than about $13°$, does not reach up to make any guiding graph nodes non-zero (a consequence of regularization).

The experiment yielding the results of Fig. 11 has the same setup, but the guiding graph is fixed with root at the center node of level 200 instead of the left-most node. The true node is varied from left to right across the plinko graph at level 210, three levels below the bottom of the guiding graph, effectively changing the center angle of the anisotropy, but leaving the extent constant. This figure is organized in the same manner as Fig. 10, but the horizontal axis features the center angle rather than angular extent. From these results, first it is apparent that only nodes in the last level of the guiding graph are non-zero, reconfirming results from the previous experiment. Second, it can be seen that when the truth is to the left of the guiding graph, the left-most node of the mth level (node a) is non-zero. Similarly, when the truth is to the right, the right node (node κ) is non-zero; when the truth is underneath the 8-level graph, nodes along the last level (nodes β-η) are non-zero.

Intuition along with these experimental validations suggests simple stopping conditions and heuristics. Two similar, but different, stopping criteria are apparent: first, stopping when all of the nodes in level m (nodes α-κ) are zero during the search, or second, stopping when in addition to all of the nodes in level m (nodes α-κ) being zero, the top node of the guiding graph (node h) is also zero. The second stopping condition is more amenable to back-tracking because it ends the search when the truth is neither above nor below the current guiding graph location. Stopping criteria of this type may terminate a search prematurely when the true anisotropy is of very small angular extent due to regularization effects seen in the first experiment, in
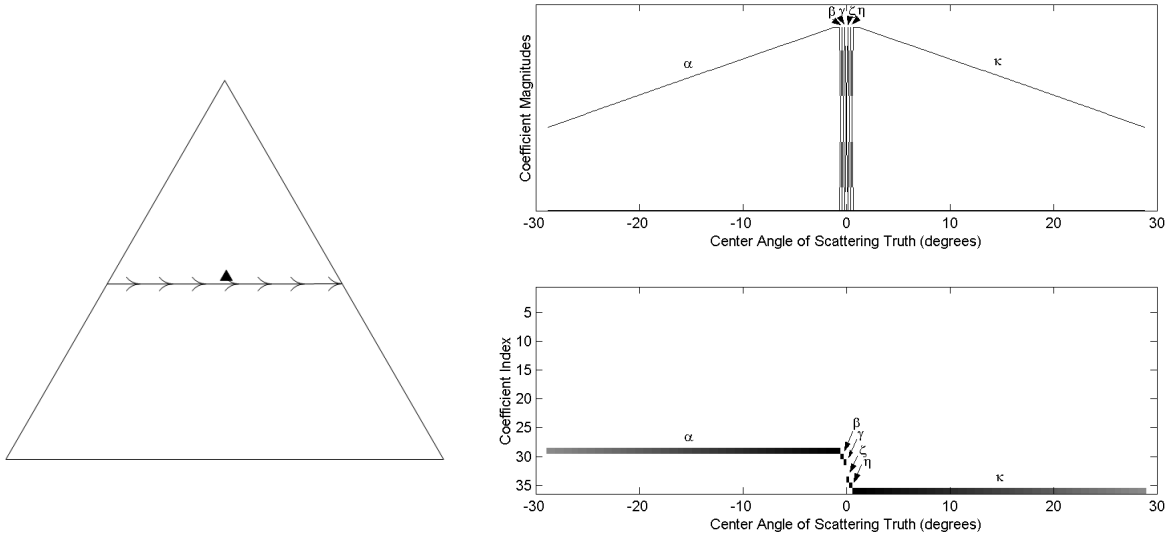
Figure 11: Coefficient magnitudes in m-level guiding graph as center angle of true scattering behavior is varied. The m-level guiding graph is fixed, covering center angles $[-1.0°, +1.0°]$.

which anisotropy of narrow angular extent resulted in all coefficients becoming zero.

A heuristic for the search is also apparent based on the coefficient values of the m nodes in level m (nodes α-κ). Due to the structure of the plinko graph, each node has two children, so the heuristic will be used to determine whether to proceed to the left child or the right child. Based on the second experiment, one reasonable idea is to compare the sum of the coefficient magnitudes in the left nodes (nodes α-δ) to the sum of the coefficient magnitudes in the right nodes (nodes ϵ-κ) — the search can then be guided towards the side with the larger sum. Stopping criteria and heuristics have now been developed for use in a heuristic search algorithm. Many other possibilities abound however. For example, the guiding graph need not be an m-level plinko graph and may be allowed to vary during the search. The basis used in calculating the given heuristic and stopping criterion has $O(1)$ columns for each spatial location and $O(P)$ columns for P spatial locations.

6.3 Hill-climbing search without back-tracking

In this section, the first approximate algorithm to join the suite of possible approximate algorithms is described and an example is given. Hill-climbing search, as described in Sec. 6.1, always finds the goal node because of back-tracking. In this first approximate algorithm, the search is limited so that back-tracking is not allowed. Consequently, there is no guarantee that the search will succeed, but the example will show that this greedy method performs well.

For the case of a single spatial location, $P = 1$, the algorithm is exactly hill-climbing search without back-tracking using the first of the stopping criteria, checking whether all coefficients of level m are zero, and the heuristic described in the previous section. The inverse problem $\mathbf{g} = \mathbf{T}^{(i)}\hat{\mathbf{f}}^{(i)} + \mathbf{n}$ is solved for each iteration i of the search. The matrix $\mathbf{T}^{(i)}$ has $N_\theta \cdot K$ rows and $\frac{1}{2}m + \frac{1}{2}m^2$ columns. Then, $\hat{\mathbf{f}}^{(i)}$ is tested for the stopping condition. If the search is to continue, the heuristic is calculated to determine which one of two choices $\mathbf{T}^{(i+1)}$ will be. The initial set of basis vectors $\mathbf{T}^{(1)}$ is the set with the largest angular extent located in the top m levels of the N_θ-level plinko graph.

For the general case of multiple spatial locations, P searches are performed simultaneously, but not
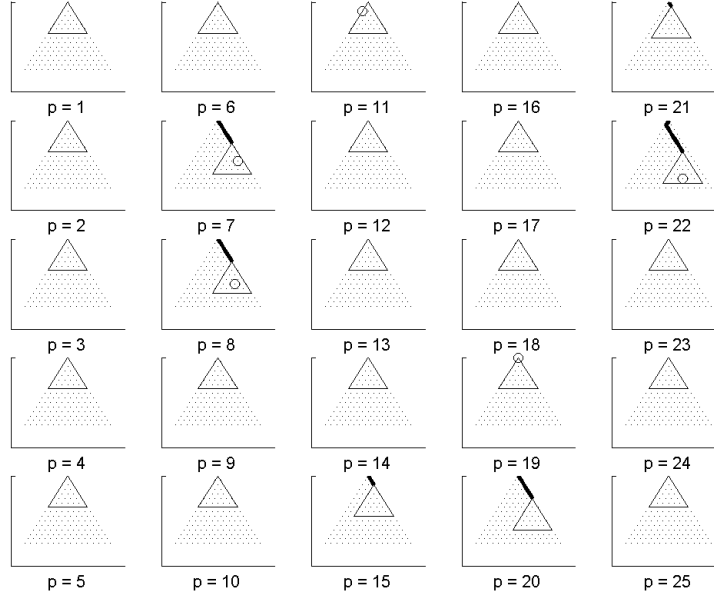
15

Figure 12: Search paths for each spatial location.

independently. As in the single location case, $\mathbf{g} = \mathbf{T}^{(i)}\hat{\mathbf{f}}^{(i)} + \mathbf{n}$ is still solved on each iteration, but now the individual block matrices $\mathbf{T}_p^{(i)}$ evolve based on their corresponding $\hat{\mathbf{f}}_p^{(i)}$. For example, the first spatial location's coefficients $\hat{\mathbf{f}}_1^{(i)}$ may satisfy the stopping condition, in which case $\mathbf{T}_1^{(i+1)} = \mathbf{T}_1^{(i)}$. The second spatial location's coefficients may indicate through the heuristic that the search should proceed to the left child, so $\mathbf{T}_2^{(i)}$ is updated accordingly. The third spatial locations coefficients may guide the search on $\mathbf{T}_3^{(i)}$ to the right child, and so on. The overall search terminates when all of the $\hat{\mathbf{f}}_p^{(i)}$ satisfy the stopping criterion. The P searches are coupled because the inverse problem is solved jointly for all spatial locations on every iteration. When there are multiple spatial locations, contributions from different positions interact, potentially leading to individual searches going in the wrong direction initially.

The first example illustrates that the greedy algorithm described above may lead to solutions comparable in quality to solutions from solving the full inverse problem at once. The setup of the scene is exactly the same as the example in Sec. 5.3 with 5 point scatterers in 25 possible locations and no additive noise. The heuristic and stopping criterion are calculated with an 8-level guiding graph, and the regularization parameter α is 4; for the stopping criterion, any coefficient magnitude less than 0.01 is considered zero. Fig. 12 shows the search paths for all 25 spatial locations as a dark solid line overlaid on the full 16-level plinko graph, with dots indicating nodes. For the 5 spatial locations with scatterers, the node corresponding to the true scattering behavior is encircled. The triangle shows the coverage of the final 8-level guiding graph for each spatial location. Fig. 13 shows the final scattering function determined by the algorithm. It is apparent in comparison with Fig. 3 that the greedy algorithm finds the solution corresponding to the underlying truth. Solving this example with the approximate algorithm took 6.5 minutes in Matlab 6 running on a 1.5 GHz Pentium processor; in comparison, the running time for solving the full inverse problem (results in Fig. 6-7) was 29.5 minutes. Looking at the search paths, despite not containing point scatterers, positions 15, 20, and 21 iterate nonetheless, but in the end correctly give all zero coefficients. Also, the searches on positions 6 and 7 do not terminate at the earliest possible opportunity, but still give correct coefficients. These effects, although not adverse to the solution in this case, are a result of the interaction between different spatial
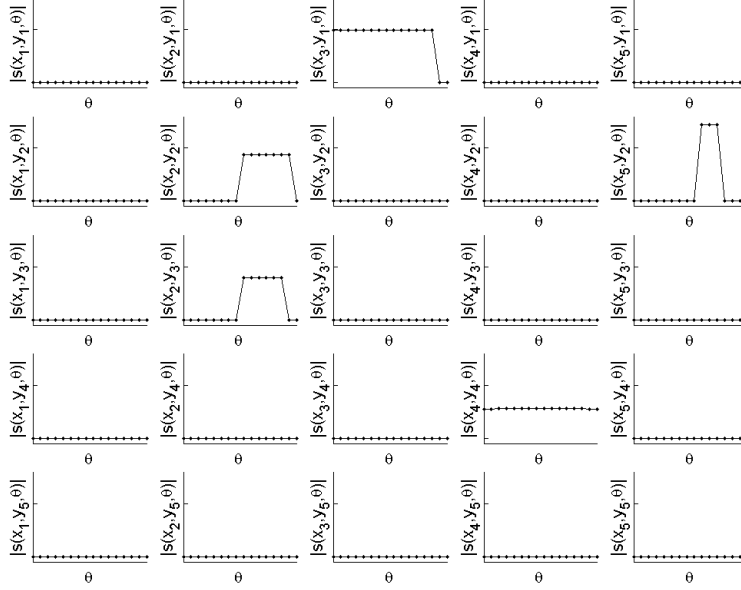
16

Figure 13: Scattering function magnitude from hill-climbing search without back-tracking.

locations and may be alleviated by including back-tracking or some other way to reduce algorithm greediness.

6.4 Removal of 'found' spatial locations

The algorithm discussed in the previous section reduces the number of basis vectors per spatial location from $O\left(N_\theta^2\right)$ to $O\left(1\right)$, but does nothing to reduce the number of spatial locations P. A further approximation can be introduced into the hill-climbing search without back-tracking to reduce the average-case dependence of the number of total basis vectors on P. It is observed that, despite interactions among contributions from different spatial locations, once the search on a particular spatial location stops it does not restart in general, but may occasionally restart after a few iterations. Fixing the contribution from a spatial location after its coefficients have been found is thus natural to consider. In the algorithm, this implies that once the stopping criterion is met at position p, the observation data $\mathbf{g}$ is updated to be $\mathbf{g}' = \mathbf{g} - \mathbf{T}_p\mathbf{f}_p$, and $\mathbf{T}_p$ is removed from matrix $\mathbf{T}$, thereby reducing the number of columns in $\mathbf{T}$. In practice, the removal is performed m iterations after the stopping criterion is met and maintained to allow for a possible restart. This algorithm is also successful at correctly solving the inverse problem, as shown in the example presented below.

The problem size in this example is larger than the examples given in Sec. 5.3 and Sec. 6.3. The range of angles is still $[-55°, +55°]$, but now there are $N_\theta = 160$ samples. The 3 frequencies and 25 spatial locations are as before, the anisotropy of the point scatterers is similar, and there is no noise. Memory constraints do not allow the full inverse problem to be solved in this case — the full $\mathbf{T}$ matrix has dimension $480 \times 322,000$. The algorithm without removal of found positions is compared to the algorithm with removal. For both, the search uses an 8-level guiding graph; for the search without removal, the regularization parameter is 12 and with removal, the regularization parameter is 15. The two search paths are given in Fig. 14, where the dotted line is the path for the algorithm without removal and the solid line is the path for the algorithm with removal. The large triangle outlines the full 160-level plinko graph. The resulting scattering function solutions are plotted in Fig. 15 along with the true scattering function. The three lines in the plots — the
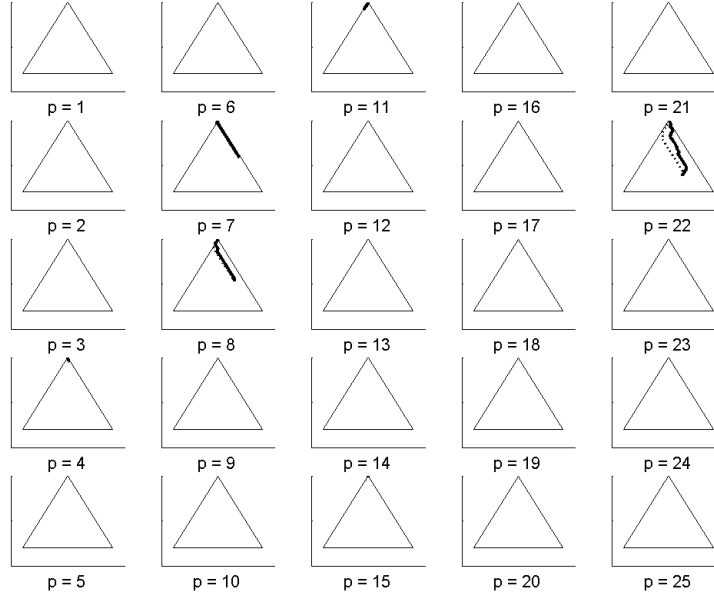
17

Figure 14: Search paths for each spatial location, where dotted line is path of algorithm without removal of found locations and solid line is path of algorithm with removal.

truth and the two solutions — are indistinguishable due to the similarity and quality of the results. Thus, a second approximate algorithm has been developed for the suite of algorithms that reduces the memory and computation requirements as a function of both N_θ and P.

6.5 Other approximations

In addition to the two approximations discussed thus far, many other options are possible that either further reduce complexity or improve performance. One way to further reduce the number of spatial locations P is through a preprocessing step that first identifies positions of interest with large scattering magnitude and only characterizes anisotropy for those positions. The justification for this preprocessing is that locations with little scattering magnitude are likely background pixels and characterizing their anisotropy is not imperative for applications. Preprocessing can be performed by first forming an image through conventional imaging or feature-enhanced imaging [4] on the full aperture or on subapertures and then thresholding or extracting peaks. Preprocessing using conventional imaging on the full aperture has proven effective on a few examples that have been looked at.

The plinko graph is structured such that in a greedy hill-climbing search without back-tracking, one wrong step eliminates many nearby nodes and paths because each node has only two children. Although good results are obtained with this structure, it can be improved. The edges of the directed acyclic graph can be modified to increase the number of children per node and consequently not disallow as many nodes and paths per search step. An example of a modified 8-level plinko graph is given in Fig. 16. A modified heuristic to go along with this modified graph is to use the m coefficients in level m of the guiding graph as before, but instead of determining whether the weighted average of the coefficient magnitudes is in the left half or the right half, determining which quarter the weighted average falls into. If the left-most quadrant is chosen, then the search proceeds to the node in the next level that is two to the left of the current node. If
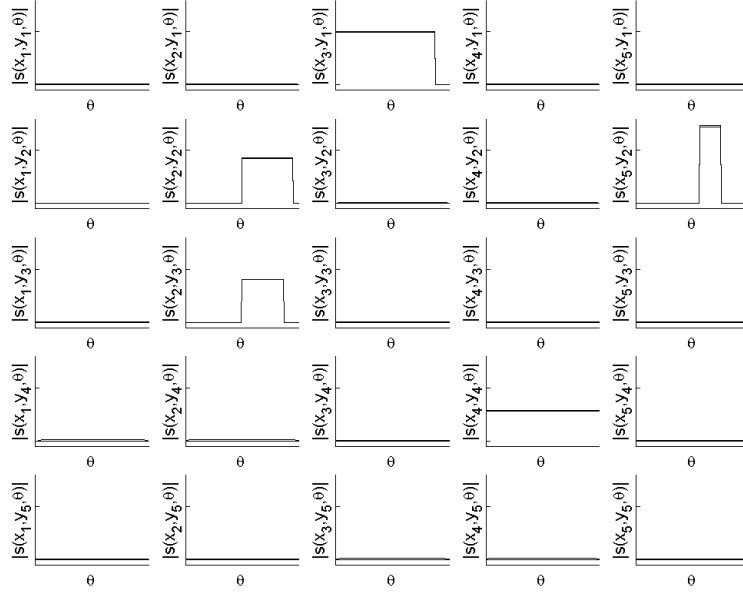
18

Figure 15: Scattering function magnitudes of truth, solution from hill-climbing search without back-tracking, and solution from hill-climbing search without back-tracking with removal of found spatial locations. The three lines are nearly indistinguishable.
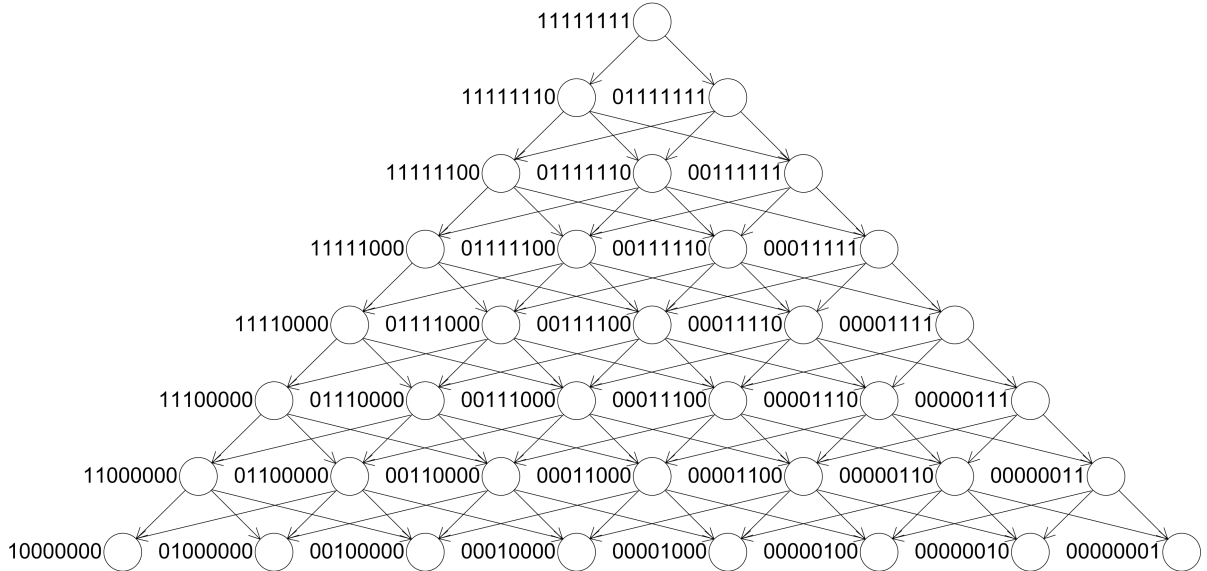

Figure 16: Modified directed acyclic graph representation for overcomplete basis.

the middle left quadrant is chosen, then the next node is one to the left in the next level, and so on. In a way, the modified plinko graph allows the search to center itself above the true node. With these additional edges, the method is less greedy with no additional cost, since calculating this modified heuristic is no more costly than calculating the original heuristic. Use of the modified plinko graph along with the modified heuristic has improved performance over the unmodified plinko graph in a number of preliminary examples that have been considered.

The search strategy discussed so far uses a single guiding graph to traverse the N_θ-level plinko graph and consequently restricts solutions to have non-zero coefficients only within the confines of the guiding graph. Many different modifications to the algorithms discussed are possible including a variety of heuristic search strategies from the literature, including strategies that allow multiple candidates in the search and multiple goal nodes, possibly through the use of multiple guiding graphs per spatial location. The methodology developed in Sec. 5 and the approximate methods in this section are a promising way to look at the anisotropy characterization problem. Directions for future research will be discussed in the next section.

7   Research directions

The research thus far has demonstrated through examples that the approach of framing the anisotropy characterization problem as an inverse problem with an overcomplete basis and sparsifying regularization shows potential. There are numerous directions yet to be explored, not the least of which is applying this method on realistic wide-angle phase history data. Some of these research directions are discussed in this section.

7.1   Larger examples and realistic datasets

The examples considered up to now have used the forward SAR model $\mathbf{T}$ and rectangular pulse anisotropy to generate the signals that are then processed, but real or realistic data has not yet been used. Processing of such data is an important next step for the research. Realistic wide-angle SAR data for scenes containing single, canonical targets such as dihedrals, trihedrals, and top hats, generated with electromagnetic prediction packages are available and will be looked at first. Use of a dataset containing 'Slicy,' a conglomeration of canonical scatterers (see Fig. 17) will also be of benefit.

Another next step in the research is to increase problem size, namely increasing N_θ, the number of angle samples, and P, the number of spatial locations, to determine whether the proposed framework and approximate algorithm continue to give promising results with such increases. Afterwards, obtaining results on large, high-resolution imaging setups with scenes containing complicated manmade targets, such as the backhoe dataset [2] (see Fig. 17), will become accessible.

7.2   Approximate algorithms

In considering algorithms in Sec. 6, the surface has only been scratched. An entire body of work on search algorithms for trees and directed acyclic graphs exists. There are many heuristic search techniques such as beam search and best first search that may yield additional algorithms for the suite of approximate algorithms. While the framework in Sec. 5 is general enough to give disparate non-zero coefficients, the hill-climbing search method will find only one non-zero coefficient. (The search algorithm may possibly give more than one, but only within the coverage of a guiding graph.) In order to transfer the generality of the framework to approximate methods, a multiple candidate algorithm that can find more than one goal node will need to be developed. Also, back-tracking in hill-climbing search has yet to be implemented and tested.

An exploration of multigrid methods [7] may provide insights and inspirations as well. The nested iteration algorithm or full multigrid, operating in a coarse-to-fine manner with corrections included, is in the same spirit as hill-climbing with back-tracking on a plinko graph, whereas one-way multigrid is similar to hill-climbing without back-tracking. Working with realistic data will guide whether these avenues of research into search and multigrid methods are worth pursuing for this specific application.
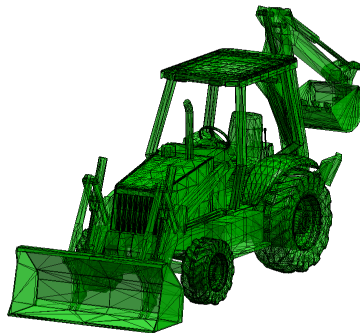
Figure 17: Slicy and backhoe targets.

7.3 Comparison to previous work

Techniques that address the characterization of anisotropic scattering in SAR have been developed in previous work, as discussed in Sec. 4, but sparsifying regularization has not yet been applied to the problem in the manner proposed. Previous methods attempt to answer a variety of questions, such as the detection of anisotropy, the extraction of angle-dependent features for automatic target recognition, the determination of the center angle of anisotropy, the determination of the angular extent of anisotropy, and the reconstruction of the full scattering function.

Metrics for performance and comparison are very dependent on which question is being answered and what the application is. The approach discussed in this proposal has not yet been compared with the other methods, but before that, fair criteria for comparison must be determined. Future work will compare the performance of the proposed method to subaperture image methods and parametric methods in the different aspects of characterizing anisotropy.

7.4 Matched bases and object-level processing

It has implicitly been assumed that rectangular functions of θ can be used to sparsely represent anisotropic scattering encountered in realistic imaging scenarios, but this conjecture has yet to be validated. Realistic data from canonical targets should provide guidance on the effectiveness of representing scattering behavior with rectangular functions. As discussed in Sec. 4, other pulse shapes such as Hamming windows, Gaussians, and shapes inspired by the geometrical theory of diffraction may be more appropriate basis vectors and can be seamlessly integrated into the proposed framework of Sec. 5. A future direction of work may be to learn a basis that sparsely represents scattering functions encountered in realistic phase history data. Learning of this sort may also lead to a basis set with fewer basis elements.

Another future direction may consider structures in the spatial domain larger in scale than points. Manmade vehicles, for example, are not arbitrary collections of point scatterers with arbitrary anisotropy. Basis elements that incorporate object-level information may be useful in this context. Object-level basis elements can represent canonical targets, for example, and be determined either from physics or by learning.

This concept has been taken to the extreme in [3], which takes the entire set of returns from a vehicle as a representer. Thus, the basis is composed of vectors such as the entire phase history from a tank, the entire phase history from a truck, and the entire phase history from a car. Such a basis set with a tank basis element, a truck basis element, etc. may be very sensitive to model mismatch. However, knowledge of target models may be exploited when put together with the algorithms in this proposal. The algorithms discussed in Sec. 6 and Sec. 7.2 are initialized at the coarsest scale, i.e. on the first iteration, each point

scatterer starts as isotropic. With an available target model, however, point scatterers can be initialized to the anisotropy specified by the model. Correction algorithms from multigrid methods can then be applied if no iteration is sought, or hill-climbing search with back-tracking or full multigrid can be applied to iterate towards a solution that removes model mismatch error.

7.5   Other topics

The work completed thus far has focused on developing a framework and some computational methods, but has stayed away from aspects such as automatic parameter selection and theoretical analysis. In the examples presented in this proposal, the regularization parameter α was chosen manually to give good results. There is a relationship between α and the size of the problem in terms of N_θ and P that has not yet been explored. The half-quadratic optimization method and its user selected parameters, a critical piece of the entire proposed work, have specifically received attention neither in relation to the full inverse problem nor to the smaller inverse problems in the approximate methods other than through examples giving reasonable results. When calculation of a search heuristic is the goal, there may be less computationally-involved alternatives for the optimization. Examination of semidefinite programming, matching pursuit, and homotopy continuation may give insights. There may also be ways to solve the full inverse problem that do not require the entire matrix $\mathbf{T}$ in memory at once.

Visualization of multidimensional scientific data is a challenge by itself. It is not a trivial exercise determining how to convey scattering function solutions $s(x, y, \theta)$ for mass publication in the absence of movies and lenticular images. The use of color, shading, and perspective plots will be considered.

The proposed research is limited to imaging with two spatial variables, but three-dimensional imaging is also an open area of research. With three dimensions, the problem changes from attempting to determine $s(x, y, \theta)$ to attempting to determine $s(x, y, z, \theta, \phi)$, where there is an additional elevation angle variable. Three-dimensional imaging will most likely not be investigated in this research.

Some simple robustness analysis has been performed with Gaussian measurement noise and small magnitude background scatterers treated as clutter, but further work is needed before meaningful conclusions can be drawn. Also, theoretical analysis of the full inverse problem and of the approximate algorithms has yet to be performed.

7.6   Timeline

A list of topics to be investigated further and specific tasks to be completed along with their expected dates of completion is given in the table below.

Task/Topic	Date of Completion
Larger-sized synthetic examples and canonical datasets	July 11
Performance metrics and comparison with other methods	August 1
Backhoe dataset	August 15
Conference 1 abstract	September 1
SSG Seminar presentation	October 1
Algorithm, analysis, examination of matching pursuit, etc.	October 15
Incorporation of object-scale information	December 15
Conference 2 extended summary	January 1
Conference 1 manuscript	March 1
S.M. Thesis	April 1
Conference 1 presentation	April 15
Conference 2 manuscript	May 1
Journal manuscript	June 1

7.7 Equipment, facilities, and data

Equipment needed for this research includes a computer outfitted with Matlab software. This equipment along with facilities will be provided by the Stochastic System Group and the Laboratory for Information and Decision Systems. Early work has used simulated data; as the research moves forward, the dataset from the Backhoe VISUAL-D Challenge Problem released by the Air Force Research Laboratory [2] will be used. Additional datasets have been obtained from SAIC, Burlington, Massachusetts.

References

[1] Mark R. Allen and Lawrence E. Hoff. Wide-angle wideband SAR matched filter image formation for enhanced detection performance. In Dominick A. Giglio, editor, *SPIE Symposium, Algorithms for Synthetic Aperture Radar Imagery*, Orlando, Florida, April 1994.

[2] Backhoe data dome and Visual-D challenge problem. Available at Air Force Research Laboratory Sensor Data Management System (https://www.sdms.afrl.af.mil/main.php), 2004.

[3] Rajan Bhalla, Junfei Li, and Hao Ling. 3-D SAR image formation from sparse aperture data using 3-D target grids. In Edmund G. Zelnio and Frederick D. Garber, editors, *SPIE Defense and Security Symposium, Algorithms for Synthetic Aperture Radar Imagery XII*, Orlando, Florida, March 2005.

[4] Müjdat Çetin and William Clem Karl. Feature-enhanced synthetic aperture radar image formation based on nonquadratic regularization. *IEEE Transactions on Image Processing*, 10(4):623–631, April 1997.

[5] Da-Ming Chiang. *Parametric signal processing techniques for model mismatch and mixed parameter estimation*. PhD thesis, The Ohio State University, Columbus, 1996.

[6] Bradley S. Denney and Rui J. P. de Figueiredo. Scattering-based tomography for HRR and SAR prediction. *Multidimensional Systems and Signal Processing*, 14(1-3):207–222, January 2003.

[7] Craig C. Douglas. Multigrid methods in science and engineering. *IEEE Computational Science and Engineering Magazine*, 3(4):55–68, Winter 1996.

[8] Laurent Ferro-Famil, Andreas Reigber, Eric Pottier, and Wolfgang-Martin Boerner. Scene characterization using subaperture polarimetric SAR data. *IEEE Transactions on Geoscience and Remote Sensing*, 41(10):2264–2276, October 2003.

[9] Layne R. Flake, Stanley Carlton Ahalt, and Ashok K. Krishnamurthy. Detecting anisotropic scattering with hidden Markov models. *IEE Proceedings - Radar, Sonar & Navigation*, 144(2):81–86, April 1997.

[10] Michael J. Gerry, Lee C. Potter, Inder J. Gupta, and Andria van der Merwe. A parametric model for synthetic aperture radar measurements. *IEEE Transactions on Antennas and Propagation*, 47(7):1179–1188, July 1999.

[11] Charles V. J. Jakowatz, Jr., Daniel E. Wahl, Paul H. Eichel, Dennis C. Ghiglia, and Paul A. Thompson. *Spotlight-Mode Synthetic Aperture Radar: A Signal Processing Approach*. Kluwer Academic Publishers, Norwell, Massachusetts, 1996.

[12] Joseph B. Keller. Geometrical theory of diffraction. *Journal of the Optical Society of America*, 52(2):116–130, February 1962.

[13] Andrew J. Kim, John W. Fisher, III, and Alan S. Willsky. Detection and analysis of anisotropic scattering in SAR data. *Multidimensional Systems and Signal Processing*, 14(1-3):49–82, January 2003.

[14] Balaji Krishnapuram, Jeffrey Sichina, and Lawrence Carin. Physics-based detection of targets in SAR imagery using support vector machines. *IEEE Sensors Journal*, 3(2):147–157, April 2003.

[15] Dmitry M. Malioutov. A sparse signal reconstruction perspective for source localization with sensor arrays. Master's thesis, Massachusetts Institute of Technology, Cambridge, Massachusetts, 2003.

[16] Randolph L. Moses, Lee C. Potter, and Müjdat Çetin. Wide angle SAR imaging. In Edmund G. Zelnio and Frederick D. Garber, editors, *SPIE Defense and Security Symposium, Algorithms for Synthetic Aperture Radar Imagery XI*, Orlando, Florida, April 2004.

[17] David C. Munson, Jr., James Dennis O'Brien, and W. Kenneth Jenkins. A tomographic formulation of spotlight-mode synthetic aperture radar. *Proceedings of the IEEE*, 71(8):917–925, August 1983.

[18] Joseph A. O'Sullivan, Richard E. Blahut, and Donald L. Snyder. Information-theoretic image formation. *IEEE Transactions on Information Theory*, 44(6):2094–2123, October 1998.

[19] Lee C. Potter and Randolph L. Moses. Attributed scattering centers for SAR ATR. *IEEE Transactions on Image Processing*, 6(1):79–91, January 1997.

[20] Paul Runkle, Lam H. Nguyen, James H. McClellan, and Lawrence Carin. Multi-aspect target detection for SAR imagery using hidden Markov models. *IEEE Transactions on Geoscience and Remote Sensing*, 39(1):46–55, January 2001.

[21] Luiz C. Trintinalia, Rajan Bhalla, and Hao Ling. Scattering center parameterization of wide-angle backscattered data using adaptive Gaussian representation. *IEEE Transactions on Antennas and Propagation*, 45(11):1664–1668, November 1997.